Extreme wave skewing and dispersion spectra of anisotropic elastic plates

Daniel A Kiefer, Sylvain Mezil, Claire Prada

▶ **To cite this version:**

Daniel A Kiefer, Sylvain Mezil, Claire Prada. Extreme wave skewing and dispersion spectra of anisotropic elastic plates. Physical Review Research, 2025, 7 (1), pp.L012043. ⟨10.1103/physrevresearch.7.l012043⟩. ⟨hal-05385783⟩

HAL Id: hal-05385783

https://hal.science/hal-05385783v1

Submitted on 27 Nov 2025

HAL is a multi-disciplinary open access archive for the deposit and dissemination of scientific research documents, whether they are published or not. The documents may come from teaching and research institutions in France or abroad, or from public or private research centers.

L'archive ouverte pluridisciplinaire **HAL**, est destinée au dépôt et à la diffusion de documents scientifiques de niveau recherche, publiés ou non, émanant des établissements d'enseignement et de recherche français ou étrangers, des laboratoires publics ou privés.

Distributed under a Creative Commons CC BY 4.0 - Attribution - International License

Letter

Extreme wave skewing and dispersion spectra of anisotropic elastic plates

Daniel A. Kiefer,* Sylvain Mezil, and Claire Prada
Institut Langevin, ESPCI Paris, Université PSL, CNRS, 75005 Paris, France

(Received 8 March 2024; revised 1 July 2024; accepted 16 January 2025; published 26 February 2025)

Guided wave dispersion is commonly assessed by Fourier analysis of the field along a line, resulting in frequency-wave-number dispersion curves. In anisotropic plates, a point source can generate multiple dispersion branches pertaining to the same modal surface, which arise due to the angle between the power flux and the wave vector. We show that this phenomenon is very particular near zero-group-velocity points and occurs in all directions independent of the degree of anisotropy. Stationary phase points accurately describe measurements on a monocrystalline silicon plate.

DOI: 10.1103/PhysRevResearch.7.L012043

Anisotropy greatly impacts guided elastodynamic wave propagation. A complication that arises is the fact that power flux is not necessarily collinear with the wave vector, a well-known effect denoted as power flux skewing [1,2]. It has traditionally been studied for nondispersive bulk and surface waves in crystals [3–8]. In monocrystalline silicon the maximum skewing angle of bulk waves is 23.7° and the one of surface waves on [001]-cut silicon is 18.1°. Recently, we have observed transverse-group-velocity (TGV) waves guided in a silicon plate [9], whose power flux is orthogonal to the wave vector, i.e., skewed ±90°. These are found in the region close to zero-group-velocity (ZGV) points, i.e., where the power flux of a mode vanishes [9]. This region naturally exhibits *extreme skewing* in that the range of skew angles covers 360°. In general, a possible consequence of skewing are multiple contributions of one mode in the overall wave field [1,4–7,10]. This usually occurs in specific propagation directions and has been attributed to *concave regions* of the wave vector surface. As such, the effect is closely linked to caustics and phonon focusing [3–5,8]. Multiplicity has been evidenced as pulses separating in time [7] and also in the form of "internal diffraction" [4,6].

In this contribution, we show that the nature of multiplicity is different in the vicinity of ZGV points, where it occurs in all directions independent of the degree of anisotropy and does not require a concave wave vector surface/contour. Guided waves in plates naturally exhibit ZGV points, and we capture the induced multiplicity by studying the effect of power flux skewing on one-dimensional (1D) scans of the wave field, which also explains the influence of the source shape on the acquired data. Using the concept of *stationary phase points*, we explain the link between the dispersion surface (frequency vs in-plane wave vector) and the *frequency-wave-number* dispersion data measured on a line. In contrast to previous work, our analysis is completely done in terms of frequency-wave vector spectra of *plane guided waves*. The model is validated against measurements on a [001]-cut monocrystalline silicon wafer, a rather weakly anisotropic material with a universal anisotropy index of AU = 0.24 [11]. Our measurements reveal strongly pronounced skewing effects, which supports our claim that the degree of anisotropy plays a minor role. Our work extends straightforwardly to other domains of linear wave propagation in anisotropic media. Analogous phenomena are expected in, e.g., (roton-like) metamaterials [12,13], phononic and photonic crystals [14–16], and polariton propagation [17,18].

The dispersive nature of guided waves in plates leads to additional complexity compared to bulk and surface waves [19,20]. Several works study low-order guided modes in strongly anisotropic composite plates with AU as high as 15.8 and skew angles generally below 60°. In this context, Velichko and Wilcox [21], Chapuis *et al.* [22], and Karmazin *et al.* [23] have successfully described the arbitrary point-to-point transmission of plate waves, thereby being interested in wave packet skewing and energy focusing. While these works were all concerned with the two-dimensional (2D) wave field in the plane of the plate, Glushkov *et al.* [24] were interested in the field along a line and explained it in terms of cylindrical guided waves. Although incomplete, 1D data are very interesting in practice because the time-consuming spatial 2D scan is avoided.

The theory of guided wave propagation in anisotropic plates is recalled briefly; for more details see [9]. The waves are characterized by their angular frequency ω and wave vector $\mathbf{k} = k\mathbf{e}_k(\theta) = k_X\mathbf{e}_X + k_Y\mathbf{e}_Y$; see Fig. 1(a). The Cartesian system $\mathbf{e}_X\mathbf{e}_Y\mathbf{e}_Z$ is fixed to the plate, while $\mathbf{e}_k\mathbf{e}_\theta\mathbf{e}_z$ is a local system oriented with the wave vector. Taking the point of view of the wave, $\mathbf{e}_k$ is denoted as the *axial direction* and $\mathbf{e}_\theta$ as the *transverse direction*. Only certain combinations of ω and $\mathbf{k}$ can propagate. The *dispersion relation* $\omega(\mathbf{k})$ forms surfaces over the Cartesian k_X-k_Y plane or, equivalently, in the cylindrical k-θ plane. It is usual to plot cuts across these surfaces for

*Contact author: daniel.kiefer@espci.fr

Published by the American Physical Society under the terms of the Creative Commons Attribution 4.0 International license. Further distribution of this work must maintain attribution to the author(s) and the published article's title, journal citation, and DOI.

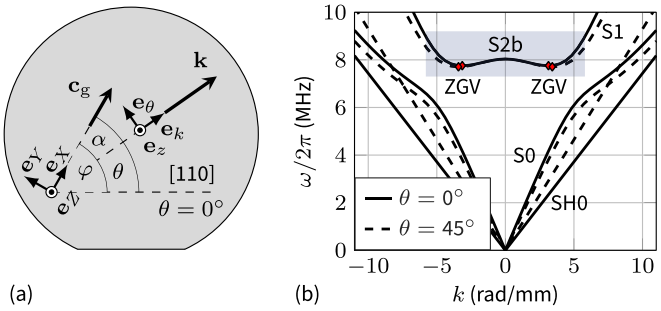

FIG. 1. Guided wave propagation in a [001]-cut monocrystalline silicon wafer. (a) Geometry in top view. Angles are defined with respect to the [110] crystal axis. θ: wave-vector orientation, φ: observation angle, α: skew angle. (b) Dispersion curves of symmetric modes for $\theta = 0°$ and $\theta = 45°$. The highlighted region of interest encompasses the S1 and S2b modes close to the ZGV points (red marks).

a chosen orientation θ of the wave vectors. Figure 1(b) shows the dispersion curves along the [110] and the [010] axes of a [001]-cut monocrystalline silicon plate with 525 µm thickness (adjusted to 524.6 µm to better match our measurements). The material's stiffness is of cubic anisotropy (Voigt-notated stiffness $C_{11} = 165.6\,\text{GPa}$, $C_{12} = 63.9\,\text{GPa}$, $C_{44} = 79.5\,\text{GPa}$, mass density $\rho = 2330\,\text{kg/m}^3$). The angle θ is commonly referred to as *propagation direction*. But for a lossless waveguide, the propagation of a wave packet is described by the group velocity vector $\mathbf{c}_\text{g}$, which might not be oriented at θ. The *group velocity* is given by [2,19]

$$\mathbf{c}_\text{g} = \nabla_\mathbf{k}\omega = \frac{\partial\omega}{\partial k}\mathbf{e}_k + \frac{1}{k}\frac{\partial\omega}{\partial\theta}\mathbf{e}_\theta\,, \tag{1}$$

and is proportional to the wave's power flux. When $\mathbf{c}_\text{g}\cdot\mathbf{k} < 0$, we speak of a *backward wave* and this is the case for the S2b mode.

In isotropic media, the second term in (1) vanishes and the group velocity is collinear to the wave vector, which justifies the notion of propagation direction. The situation is different in anisotropic plates. While $\mathbf{k}$ is oriented at angle θ, $\mathbf{c}_\text{g}$ is at angle φ. The difference, $\alpha = \varphi - \theta$, is denoted as *steering* or *skew angle* [2,22,23]. The angle φ dictates the observability of the corresponding wave component. To explain this, assume a source at the origin of $\mathbf{e}_X\mathbf{e}_Y\mathbf{e}_Z$ and a point of interest at $X\mathbf{e}_X$, where $\mathbf{e}_X$ is the *observation direction*. Waves with group velocity $\mathbf{c}_\text{g}$ oriented along $\mathbf{e}_X$ are denoted as *stationary phase points* [22–24] and only these waves contribute to the field at $X\mathbf{e}_X$ (disregarding evanescent waves). In fact, expanding the wave field with this set of propagating modes is equivalent to a stationary phase approximation of the far field [22].

Our goal is to model and identify waves measured on a line away from a source. Which waves are observed depends on the source in two ways: (i) the wave-vector spectrum that it excites, and (ii) its aperture, which defines a range of observation directions for each point on the scan line. To understand the differences between the extreme cases of a point source and a line source, we sketch the excitation of a single mode at a given frequency in Fig. 2. The line source excites mostly two wave vectors collinear with the observation direction. Although the skewed power flux inclines the radiated beam,

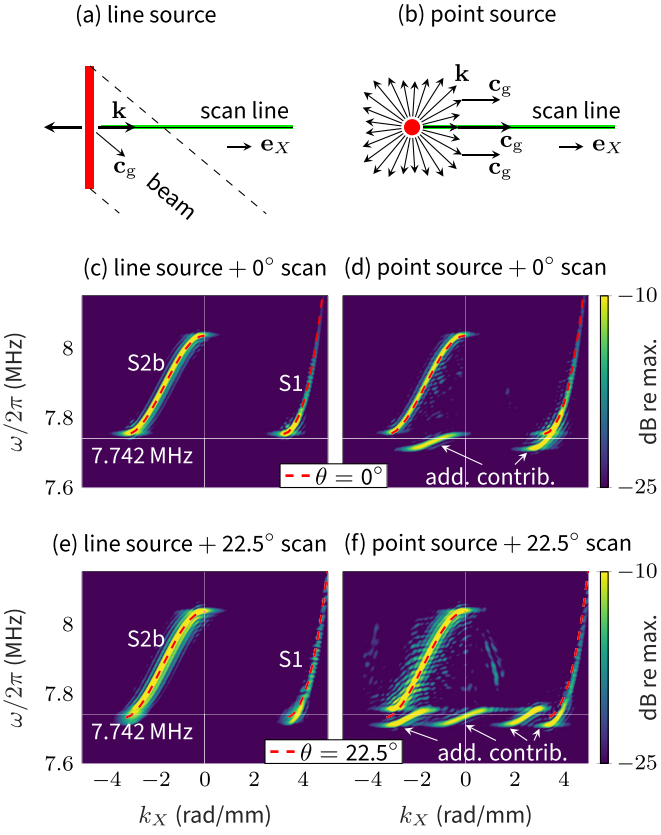

FIG. 2. Line source vs point source on an anisotropic plate. (a) The line source excites (mostly) two wave vectors, and the emitted beam is skewed. (b) The point source excites a broad spectrum of wave vectors, and some of them are observable along the scan line. (c), (d) Corresponding spectra of the out-of-plane surface displacements measured along the [110] axis of a silicon plate. (e), (f) Same as (c), (d) but scanned at 22.5° out of the [110] axis.

the wave is nonetheless observed on the scan line thanks to the extend (aperture) of the source. As expected, the measured wave number will be $k_X = \mathbf{k}\cdot\mathbf{e}_X = k$ because $\mathbf{e}_k = \mathbf{e}_X$. This means that the acquired dispersion data are correctly explained by the theoretical dispersion curves of Fig. 1(b). Because of the finite length of the source, the wave can be measured only within a section of the scanned line, as seen in Fig. 2(a). Hence, we expect a skew angle-dependent broadening of the acquired wave-number spectrum.

Measurements are performed with a laser-ultrasonic setup similar to Ref. [9]. It consists of a pulsed laser source (10-ns duration, 1064-nm wavelength) and an interferometer (532-nm wavelength) that measures the surface normal displacements. The source forms either a ≈7 mm-long line or a small spot on the plate's surface, with 4.5 mJ and 3 mJ energy, respectively. Both sources excite wave numbers up to $k \approx 20\,\text{rad/mm}$. The scan is performed on a 40-mm-long line away from the source by displacing the interferometer with a translation stage in steps of 0.1 mm. The temporal acquisition is 100 µs long. A spatiotemporal Fourier transform with a 20%-tapered cosine window in both dimensions yields the spectra depicted in Figs. 2(c)–2(f). With a line source, both the scan along $\varphi = 0°$ [Fig. 2(c)] and the one at $\varphi = 22.5°$

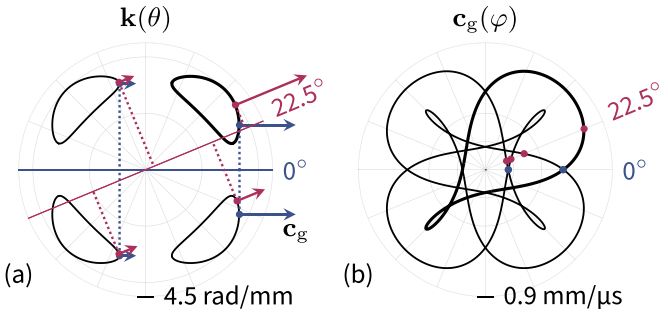

FIG. 3. Cuts at 7.742 MHz of (a) the dispersion surface and (b) the ray surface. The modes observable at 0° and 22.5° are marked therein. The wave vector projections (dotted line) onto the corresponding direction (solid line) were measured in Figs. 2(d) and 2(f).

[Fig. 2(e)] show excellent agreement to the dispersion curves computed for $\theta = 0^\circ$ and $\theta = 22.5^\circ$, respectively. Note that $\theta = 0^\circ$ is a symmetry axis, and the corresponding skew angles are zero, while this is not the case for $\theta = 22.5^\circ$. The mentioned skew-dependent broadening is confirmed when comparing Fig. 2(e) to Fig. 2(c).

The point source sketched in Fig. 2(b) excites wave vectors in all possible directions θ. Due to anisotropy, these wave vectors $\mathbf{k}$ exhibit different magnitudes and associated group velocities $\mathbf{c}_g$. Certain specific modes will have $\mathbf{c}_g$ directed along the scan line and are hence measured. The experimentally acquired wave numbers are the projection of these wave vectors onto the observation direction, i.e., $k_X = \mathbf{k} \cdot \mathbf{e}_X = k \cos\alpha$. This explains the discrepancy in Fig. 2(f) with respect to the superposed dispersion curves computed for $\theta = 22.5^\circ$, in particular, close to the minimum in frequency. Most remarkably, multiple $\mathbf{k}$ might propagate energy in the chosen observation direction, leading to the mentioned multiplicity. As seen in Figs. 2(d) and 2(f), this manifests in additional dispersion branches that also pertain to the S1 and S2b modes.

While the sketch in Fig. 2(b) is qualitative, in Fig. 3 we plot the actual isofrequency contour $\mathbf{k}(\theta)$ and ray contour $\mathbf{c}_g(\varphi)$ at 7.742 MHz. Note that $\mathbf{c}_g$ is always normal to the isofrequency contours. For both measurement directions, we marked the corresponding four stationary phase points, i.e., plane waves that propagate energy in the observation direction. They explain the additional contributions in Figs. 2(d) and 2(f). Note that only two of the solutions are actually observed for the 0° scan because two pairs of points exhibit the same k_X. The number of stationary phase points varies with the scan angle. Figure 3(b) exhibits six of them in a narrow range close to 45°. This is due to the small loops in the ray contours that can be attributed to the concave regions in the dispersion contours. In the following, we analyze the frequency dependence of the acquired response while restricting to the case of a point source. The results are applicable to any source distribution via Fourier analysis.

The full dispersion surface of the S1 and S2b modes is depicted in the form of isofrequency contours in Fig. 4(a). The modes exhibit four ZGV points on $\theta = 45^\circ + n \times 90^\circ$, $n \in \mathbb{Z}$ ($\langle 100 \rangle$ axes) that correspond to minima of the dispersion surface and are denoted as ZGV1 (marked as e, e′, c and c′) [9]. Additionally, it exhibits four ZGV points on $\theta = n \times 90^\circ$ ($\langle 110 \rangle$ axes) that correspond to saddle points (b, b′, d, d′). The latter are at a slightly higher frequency and are denoted as ZGV2. For θ outside symmetry axes, the minimum in the dispersion curve corresponds to a TGV wave, i.e., its power flux is orthogonal to the wave vector. The dashed curve in Fig. 4(a) marks the loci of TGV waves [9].

A point source excites modes on the entire dispersion surface. The loci of the wave vectors that can be measured right (left) to the source are marked on the dispersion surface of Fig. 4(a) as dark (light) green points. As $\mathbf{c}_g$ is normal to the isofrequency contours, these stationary phase points correspond to the locations where the contours are vertical. The horizontal [110] axis is a reflection symmetry axis that coincides with the observation direction and all points on this line are stationary phase points. Additional stationary phase points are found close to the TGV waves. First, the isofrequency contours close to a ZGV1 point (minimum) encircle this point away from the origin. This implies one off-axis point where $\mathbf{c}_g$ is oriented along $\mathbf{e}_X$ and one where it is along $-\mathbf{e}_X$, as is indicated on the highlighted convex contours. Second, the ZGV2 points (saddle points) induce regions where the surface is concave (e.g., between b′ and g). Therefore, the ZGV2 point at 0° (180°) leads to two symmetric stationary phase points for observation along $+\mathbf{e}_X$ ($-\mathbf{e}_X$). The ZGV points and the thickness resonance at $k = 0$ rad/mm are always stationary phase points, and it is here that the group velocity $\mathbf{c}_g$ changes direction.

Projecting the stationary phase points onto the ω-k_X plane and plotting them as conventional frequency-wave-number dispersion curves leads to the representation in Fig. 4(b). We observe two curves in "W" shape. While the upper "W" is due to the points on the horizontal axis of the dispersion surface of Fig. 4(a), the lower one is due to the points encircling the center. We remark that only the projection of the latter onto the observation direction is measured, meaning *a priori* that the wave vector magnitude k remains unknown. As the lower and the upper stationary phase points of the circle in Fig. 4(a) have the same k_X, they merge in the lower "W" curve of Fig. 4(b). This manifests in coalescence of the eight stationary phase points marked in Fig. 4(a) into four points in Fig. 4(b). We remark that the lower "W" has an upper cutoff frequency marked by a cross. It is given by point g on the dispersion contours, and above this frequency the contours become purely convex. In contrast to Fig. 2, we now scanned *across the source* with a distance of 40 mm to each side. This is why we obtain the symmetric spectrum ($\varphi = 0^\circ$ and $\varphi = 180^\circ$) seen in Fig. 4(c). The theoretical predictions are superposed on the measurements and the agreement is remarkably good.

Next, to measure along a line that is not a symmetry axis, we rotate the plate by -22.5° while keeping the observation directions $\pm\mathbf{e}_X$ horizontal. The stationary phase points for the rotated material are marked on the dispersion surface of Fig. 4(d). They form an "S"-shaped path. Figure 4(e) shows the corresponding frequency-wave-number dispersion forming twisted curves with up to eight different wave numbers per frequency (or up to three frequencies per wave number). These points are highlighted for one frequency in Figs. 4(d) and 4(e). Four of them pertain to the S1 mode (outside the TGV curve), while the other four are associated

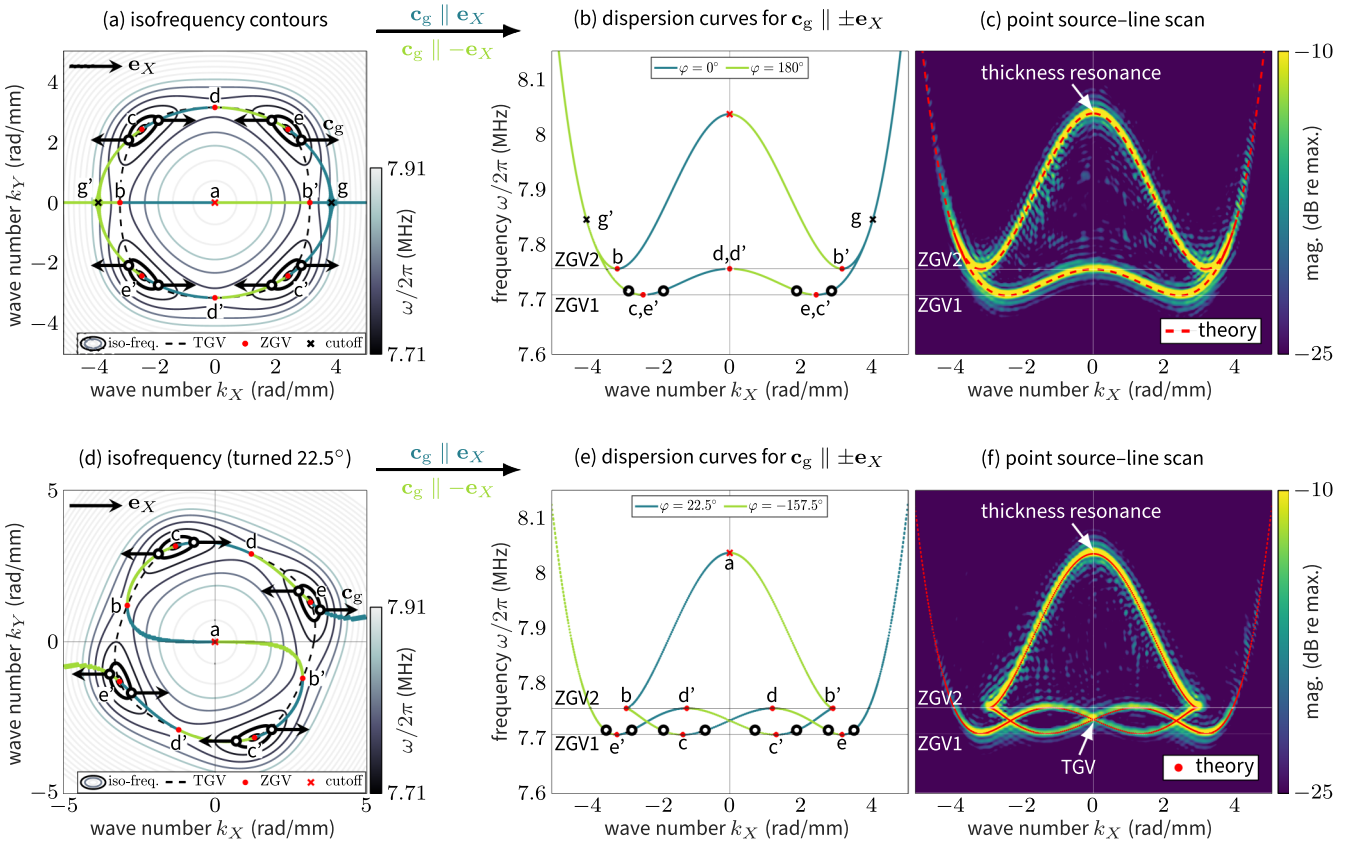

FIG. 4. Waves observable with a point source and a line scan along $\mathbf{e}_X$. The top row (a)–(c) is for a scan along the [110] axis ($\varphi = 0°$), while the bottom row (d)–(f) is for a scan at angle $\varphi = 22.5°$. (a), (d) Dispersion surface of the S1/S2b modes as isofrequency contours oriented such that the observation direction $\mathbf{e}_X$ is horizontal. The stationary phase points marked therein in dark (light) green are the waves observable to the right (left) of the source. Observable group velocity vectors are sketched for one selected frequency. (b), (e) Stationary phase points as frequency $\omega/2\pi$ vs horizontal wave number k_X. The highlighted points from (a) and (d) are also marked. (c), (f) Measured spectral magnitude obtained by scanning across the point source vs the theoretical stationary phase points from (b) and (e).

to the S2b mode (inside the TGV curve). Like previously, the waves observable to the right (left) correspond to the branches with positive (negative) slope in Fig. 4(e). The corresponding experimental dispersion curves are depicted in Fig. 4(d) and are seen to coincide again with the theoretical predictions.

To the best of our knowledge, no algorithm has been devised to directly compute the stationary phase points. As a work around, we have computed the dispersion surface of the S1/S2b modes on a dense set of about 2.1 million (k, θ) points. Subsequently, we selected the solutions where $\mathbf{c}_g$ is in the desired direction within 2 mrad (≈0.1°) tolerance. The computation was done with our open source software `GEWtool` [25] and takes about 1.5 min using eight cores of an Apple M1 Pro processor.

In conclusion, the frequency-wave-number spectra obtained by scanning a line away from a source on an anisotropic elastic plate is explained by the stationary phase points on the dispersion surface. ZGV points entail the unfolding of a mode into multiple well-resolved contributions in the experimentally acquired line-scan spectra. This was validated by measurements on a monocrystalline silicon wafer, a rather weakly anisotropic material. Furthermore, the extreme power flux skewing induced by the ZGV points implies that wave vectors spanning 360° contribute to the data acquired in a single arbitrary direction away from a point source. This phenomenon opens perspectives for the inverse characterization of complex anisotropic materials with limited data [26,27], as it inherently contains directional information. Other applications where we anticipate great benefits include microelectromechanical sensors and filters [28], nondestructive testing, and structural health monitoring [10].

The authors are thankful to Daniel Royer and Fabrice Lemoult for their helpful comments. This work has received support under the program "Investissements d'Avenir" launched by the French Government under Reference No. ANR-10-LABX-24.

[1] B. A. Auld, *Acoustic Fields and Waves in Solids*, 2nd ed. (Krieger, Malabar, FL, 1990), Vol. 1.

[2] K.-J. Langenberg, R. Marklein, and K. Mayer, *Ultrasonic Nondestructive Testing of Materials: Theoretical Foundations* (CRC Press, Boca Raton, FL, 2012).

[3] A. G. Every, W. Sachse, K. Y. Kim, and M. O. Thompson, Phonon focusing and mode-conversion effects in silicon at ultrasonic frequencies, Phys. Rev. Lett. **65**, 1446 (1990).

[4] M. R. Hauser, R. L. Weaver, and J. P. Wolfe, Internal diffraction of ultrasound in crystals: Phonon focusing at long wavelengths, Phys. Rev. Lett. **68**, 2604 (1992).

[5] A. G. Every, Formation of phonon-focusing caustics in crystals, Phys. Rev. B **34**, 2852 (1986).

[6] R. E. Vines, S.-I. Tamura, and J. P. Wolfe, Surface acoustic wave focusing and induced Rayleigh waves, Phys. Rev. Lett. **74**, 2729 (1995).

[7] A. A. Maznev, A. M. Lomonosov, P. Hess, and A. A. Kolomenskii, Anisotropic effects in surface acoustic wave propagation from a point source in a crystal, Eur. Phys. J. B **35**, 429 (2003).

[8] A. G. Every, A. A. Maznev, W. Grill, M. Pluta, J. D. Comins, O. B. Wright, O. Matsuda, W. Sachse, and J. P. Wolfe, Bulk and surface acoustic wave phenomena in crystals: Observation and interpretation, Wave Motion **50**, 1197 (2013).

[9] D. A. Kiefer, S. Mezil, and C. Prada, Beating resonance patterns and extreme power flux skewing in anisotropic elastic plates, Sci. Adv. **9**, eadk6846 (2023).

[10] W. Duan and T.-H. Gan, Investigation of guided wave properties of anisotropic composite laminates using a semi-analytical finite element method, Compos. B Eng. **173**, 106898 (2019).

[11] S. I. Ranganathan and M. Ostoja-Starzewski, Universal elastic anisotropy index, Phys. Rev. Lett. **101**, 055504 (2008).

[12] A. Bossart and R. Fleury, Extreme spatial dispersion in nonlocally resonant elastic metamaterials, Phys. Rev. Lett. **130**, 207201 (2023).

[13] K. Wang, Y. Chen, M. Kadic, C. Wang, and M. Wegener, Nonlocal interaction engineering of 2D roton-like dispersion relations in acoustic and mechanical metamaterials, Commun. Mater. **3**, 35 (2022).

[14] J. H. Page, Focusing of ultrasonic waves by negative refraction in phononic crystals, AIP Adv. **6**, 121606 (2016).

[15] M. Notomi, Theory of light propagation in strongly modulated photonic crystals: Refractionlike behavior in the vicinity of the photonic band gap, Phys. Rev. B **62**, 10696 (2000).

[16] J. D. Joannopoulos, S. G. Johnson, J. N. Winn, and R. D. Meade, *Photonic Crystals: Molding the Flow of Light*, 2nd ed. (Princeton University Press, Princeton, 2008).

[17] E. Galiffi, G. Carini, X. Ni, G. Álvarez-Pérez, S. Yves, E. M. Renzi, R. Nolen, S. Wasserroth, M. Wolf, P. Alonso-Gonzalez, A. Paarmann, and A. Alù, Extreme light confinement and control in low-symmetry phonon-polaritonic crystals, Nat. Rev. Mater. **9**, 9 (2024).

[18] X. Zhang, Q. Yan, W. Ma, T. Zhang, X. Yang, X. Zhang, and P. Li, Ultrafast anisotropic dynamics of hyperbolic nanolight pulse propagation, Sci. Adv. **9**, eadi4407 (2023).

[19] B. A. Auld, *Acoustic Fields and Waves in Solids*, 2nd ed. (Krieger, Malabar, FL, 1990), Vol. 2.

[20] D. Royer and T. Valier-Brasier, *Elastic Waves in Solids 1: Propagation* (ISTE and John Wiley & Sons, New York, 2022).

[21] A. Velichko and P. D. Wilcox, Modeling the excitation of guided waves in generally anisotropic multilayered media, J. Acoust. Soc. Am. **121**, 60 (2007).

[22] B. Chapuis, N. Terrien, and D. Royer, Excitation and focusing of Lamb waves in a multilayered anisotropic plate, J. Acoust. Soc. Am. **127**, 198 (2010).

[23] A. Karmazin, E. Kirillova, W. Seemann, and P. Syromyatnikov, A study of time harmonic guided Lamb waves and their caustics in composite plates, Ultrasonics **53**, 283 (2013).

[24] E. Glushkov, N. Glushkova, A. Eremin, and R. Lammering, Group velocity of cylindrical guided waves in anisotropic laminate composites, J. Acoust. Soc. Am. **135**, 148 (2014).

[25] D. A. Kiefer, GEWtool (2025), doi:10.5281/zenodo.10114243, https://github.com/dakiefer/GEWtool.

[26] M. Thelen, N. Bochud, M. Brinker, C. Prada, and P. Huber, Laser-excited elastic guided waves reveal the complex mechanics of nanoporous silicon, Nat. Commun. **12**, 3597 (2021).

[27] M. Ponschab, D. A. Kiefer, and S. J. Rupitsch, Simulation-based characterization of mechanical parameters and thickness of homogeneous plates using guided waves, IEEE Trans. Ultrason. Ferroelectr. Freq. Control **66**, 1898 (2019).

[28] V. Yantchev, L. Arapan, I. Katardjiev, and V. Plessky, Thin-film zero-group-velocity Lamb wave resonator, Appl. Phys. Lett. **99**, 033505 (2011).